remote sensing

MDPI

Article

Predicting Fuel Moisture Codes Across Mountainous Forests of British Columbia Using L-Band ALOS-2 PALSAR-2 Imagery

Marin Loncar [1], Brigitte Leblon [1,*], Ashlin Richardson [2], Laura Bourgeau-Chavez [3] and Dzhamal Amishev [1]

[1] Faculty of Natural Resources Management, Lakehead University, Thunder Bay, ON P7B 5E1, Canada; mloncar@lakeheadu.ca (M.L.); damish15@lakeheadu.ca (D.A.)
[2] British Columbia Wildfire Service, Victoria, BC V8W 9C1, Canada; ashlin.richardson@gov.bc.ca
[3] Michigan Tech Research Institute, Michigan Technological University, Ann Arbor, MI 48105, USA; lchavez@mtu.edu
* Correspondence: bleblon@lakeheadu.ca

Highlights

What are the main findings?

- Polarimetric synthetic aperture radar data derived from terrain-corrected ALOS-2 PALSAR-2 L-band images obtained from sparse sites predicted the Drought Code and Duff Moisture Code with moderate accuracy.
- Drought Code values are predicted more accurately than the Duff Moisture Code over forest sites, but it is the opposite over unforested sites.

What are the implications of the main findings?

- Terrain-corrected L-band polarimetric SAR data may identify spatial variability in fuel moisture codes that are not represented by seasonal trends or point-based weather observations.
- Applications of DC and DMC models will require multi-year SAR data to be combined with vegetation, soil, and surface structure data to account for spatial differences across heterogeneous environments.

Abstract

Fuel moisture codes are numerical indices used to estimate the moisture content of different layers of forest fuels and are widely applied to assess the ignition potential and behavior of wildfires. Terrain-corrected L-band ALOS-2 PALSAR-2 synthetic aperture radar (SAR) imagery predicted the Drought Code (DC) and Duff Moisture Code (DMC) of the Canadian Forest Fire Danger Rating System in mountainous forests of British Columbia. Random forest regression models were developed using backscatter, decomposition parameters, and polarimetric discriminators obtained from forest (high-biomass, conifer-dominated), sparse (medium-biomass, open canopy), and unforested (low-biomass, herbaceous-dominated) fuel types near weather stations. Out-of-bag predicted values were compared against weather station-derived values. Models trained using SAR data predicted the DC with moderate accuracy in sparse (R^2 = 0.49, RMSE = 165.65) and forest sites (R^2 = 0.39, RMSE = 173.80), and with low accuracy in unforested sites (R^2 = 0.15, RMSE = 205.96). Models trained using SAR data predicted the DMC with moderate accuracy in sparse (R^2 = 0.64, RMSE = 26.07) and unforested sites (R^2 = 0.47, RMSE = 31.52), and with low accuracy in forest sites (R^2 = 0.12, RMSE = 40.71). Incorporating SAR data and day of year (DOY) improved the accuracy of DC models. Errors in both DC and DMC increased when models were evaluated with SAR data from weather stations not used in training, suggesting limited spatial transferability beyond training weather stations. Results suggest

Check for updates

Academic Editor: Ioannis Gitas

Received: 13 July 2026
Revised: 23 September 2026
Accepted: 3 November 2026
Published: 6 November 2026

Copyright: © 2026 by the authors. Licensee MDPI, Basel, Switzerland. This article is an open access article distributed under the terms and conditions of the Creative Commons Attribution (CC BY) license.

that terrain-corrected L-band polarimetric SAR has potential for predicting fuel moisture in mountainous and forested environments. Differences in surface and soil conditions across the fire environment must be accounted for to improve the spatial transferability of the models.

Keywords: polarimetric SAR; fuel moisture; wildfire; random forest; ALOS-2; Drought Code; Duff Moisture Code; fire danger; Fire Weather Index

1. Introduction

The Canadian Forest Fire Danger Rating System (CFFDRS) is an essential tool used to inform decision-making and maximize the effectiveness of wildfire management across Canada and around the world [1,2]. It delivers critical predictions required to determine resource placements, alert statuses, suppression strategies, and threats to human safety and property [3]. The CFFDRS has a Fire Occurrence Prediction (FOP) subsystem that predicts daily fire occurrence with lightning and human risk models [4]. The Fire Behaviour Prediction (FBP) system is the second subsystem of the CFFDRS. It predicts fire behavior variables, such as rate of spread, fuel consumption, and fire intensity, from site-specific factors of the fire environment, such as fuel and topography [5]. Both subsystems use as inputs the outputs from the third CFFDRS subsystem, namely the Fire Weather Index (FWI), which gives daily measures of general fire danger [6].

The FWI uses data on the amount of fuel available for combustion (Buildup Index; BUI) and spread potential following ignition (Initial Spread Index; ISI). The BUI and ISI are calculated by considering codes related to the moisture content of three types of dead forest fuel. The first one is the Fine Fuel Moisture Code (FFMC), which describes the moisture content of fine surface litter (fast drying with a time lag of 2/3 of a day) that is related to the spread rate of a fire. The second one is the Duff Moisture Code (DMC), which represents the moisture content of medium-size fuels consisting of moderately deep, loosely compacted organic fuel (moderate drying with a time lag of 12 days). It is important for assessing fire ignition potential and intensities. The third one is the Drought Code (DC), which measures the moisture content of the deep, compact organic soil and large fuels (slow drying with a time lag of 52 days). DC is related to fire intensity, the depth of burn, and the difficulty of extinguishment. The three moisture codes are computed from daily measurements of wind, temperature, humidity, and precipitation.

Given that the CFFDRS relies on point-source weather data, its accuracy is largely limited by how well the fuel and weather conditions (current and historical) can be described at any given location [7]. Weather data are interpolated with high uncertainty between weather stations that are sometimes distant by hundreds of km [8]; hence, they cannot account for differences at fine spatial scales. An accurate capture of local moisture variability requires spatially accurate, large-footprint, and repeatable data. Such data can be provided by remote sensing tools, such as spaceborne synthetic aperture radar (SAR) systems [9,10], which interact with forest fire fuels and are sensitive to moisture [11].

Relationships between DMC, DC, BUI, and backscatter in the C-HH and C-VV polarizations have been identified [12–14]. Polarimetric SAR systems were also used to estimate rainfall [12], soil moisture [15,16], and live fuel moisture [17,18]. Variables derived from polarimetric data obtained from C-band systems, such as backscatter in linear and circular polarizations, and parameters of the Freeman–Durden [19] and Van Zyl [20] Decompositions have been observed to significantly differ between DC values [21]. Moisture prediction models that include multiple polarimetric variables as inputs have isolated the effects of

fuel moisture on SAR data by accounting for differences in fuel type, structure, or surface roughness across a landscape [22].

Previous research on SAR-based fuel moisture monitoring focused mainly on low-biomass and topographically flat regions using data obtained from C-band SAR systems [12–15,21,22]. The diverse fire environment of Canada requires fuel moisture codes to be also monitored in mountainous and high-biomass environments, which present additional challenges. Data obtained from C-band systems are only sensitive to DC in low-biomass environments due to high attenuation by live above-ground biomass [22]. A longer wavelength, which interacts less with above-ground biomass such as L-band, is required to measure moisture in high-biomass forested environments [23].

Fuel moisture prediction methods that were previously developed in flat landscapes are unable to be replicated across mountainous areas because SAR data is distorted by sloped terrain [24]. Effects include undulations in backscatter resulting from differences in incident angles and the local area illuminated by a SAR pulse, shifts in the polarization orientation angle (POA) between the polarization and horizontal axes, and distortions in the spatial positioning of pixels [25]. Applying SAR to fuel moisture monitoring in mountainous environments requires the application of a three-step terrain correction to the processing workflow of the SAR data to reduce the effects of slopes [25,26] and increase the likelihood that the effects of fuel moisture on the data can be detected. This includes (1) radiometric terrain flattening using a digital elevation model (DEM), which normalizes backscatter by the local ground area contributing to each radar cell into a terrain-flattened gamma nought (γ^o) notation product [27]. (2) The rotation of the POA is estimated and removed from the polarimetric coherency matrix [28,29]. (3) The location of each pixel in the SAR image is shifted to its real-world location using a DEM and geocoded into a map coordinate system [30].

Optimal polarimetric variables for use in fuel moisture modelling have been previously identified by comparing terrain-corrected data obtained from two L-band images that differed in DC [31]. Variables that were observed to differ between drier and wetter conditions may be advantageous in predicting fuel moisture. These include backscatter in linear and circular polarizations, the parameters of the Van Zyl Decomposition, the total power (span), maximum and minimum of scattering intensity (S-max, S-min), the maximum of power received (Pr-max), the maximum and minimum of the completely polarized component (Pol-max, Pol-min), and the maximum of the completely unpolarized component (UnPol-max) [32–34]. Variables that do not change as DC changes may be used to decouple moisture from other surface factors [35]. These include the parameters of the Cloude–Pottier [36] and Neumann Decompositions [37], and the fractional polarization (FP). Although empirical relationships between DC and polarimetric variables derived from terrain-corrected data obtained from L-band images have been studied, fuel moisture prediction models incorporating this data have yet to be developed.

This study uses terrain-corrected L-band ALOS-2 PALSAR-2 imagery to model the DC and DMC in mountainous forests of southeast British Columbia (BC). The FFMC was not modelled because the revisit time of ALOS-2 PALSAR-2 cannot capture rapid fluctuations in FFMC that can occur with daily weather conditions. Polarimetric SAR variables, including backscatter, decomposition parameters, and polarimetric discriminators, are extracted from target areas located within the immediate footprints of three BC Wildfire Service weather stations and compared to station-derived DC and DMC values. Random forest (RF) regression models are developed to predict the DC and DMC using data from three general fuel types: forest (high-biomass, conifer-dominated), sparse (medium-biomass, open canopy), and unforested (low-biomass, herbaceous-dominated) that are representative of BC. This study develops the first application of terrain-corrected L-band polarimetric

SAR to predict the DC and the DMC to inform wildfire preparedness and response at much finer spatial resolutions than are possible using weather stations.

2. Materials and Methods

2.1. Study Area

The 2800 km^2 study area surrounds the town of Windermere, BC, Canada (Figure 1; 50°27′45″N, 115°59′19″W). The area is highly mountainous, ranging from 745 m to 3389 m above sea level. Land cover is predominantly forests of the Interior Douglas Fir, Montane Spruce, Engelmann Spruce–Subalpine Fir, and Interior Cedar–Hemlock biogeoclimatic zones. Sparse forests with intermittent tree cover occur throughout in isolated patches. Unforested areas occur mainly in large, grass-dominated valley sites and to a lesser extent in smaller recently harvested areas. Barren land devoid of vegetation occurs at high-elevation mountain tops. The towns of Radium, Invermere, Windermere, Fairmont Hot Springs, and Canal Flats are in the westernmost valley. Three BCWS weather stations exist within the study area: Toby Hub (50°30′46″N, 116°03′19″W, 1180 m), Palliser (50°29′41″N, 115°39′59″W, 1030 m), and Emily Creek (50°08′42″N, 115°58′38″W, 1180 m).

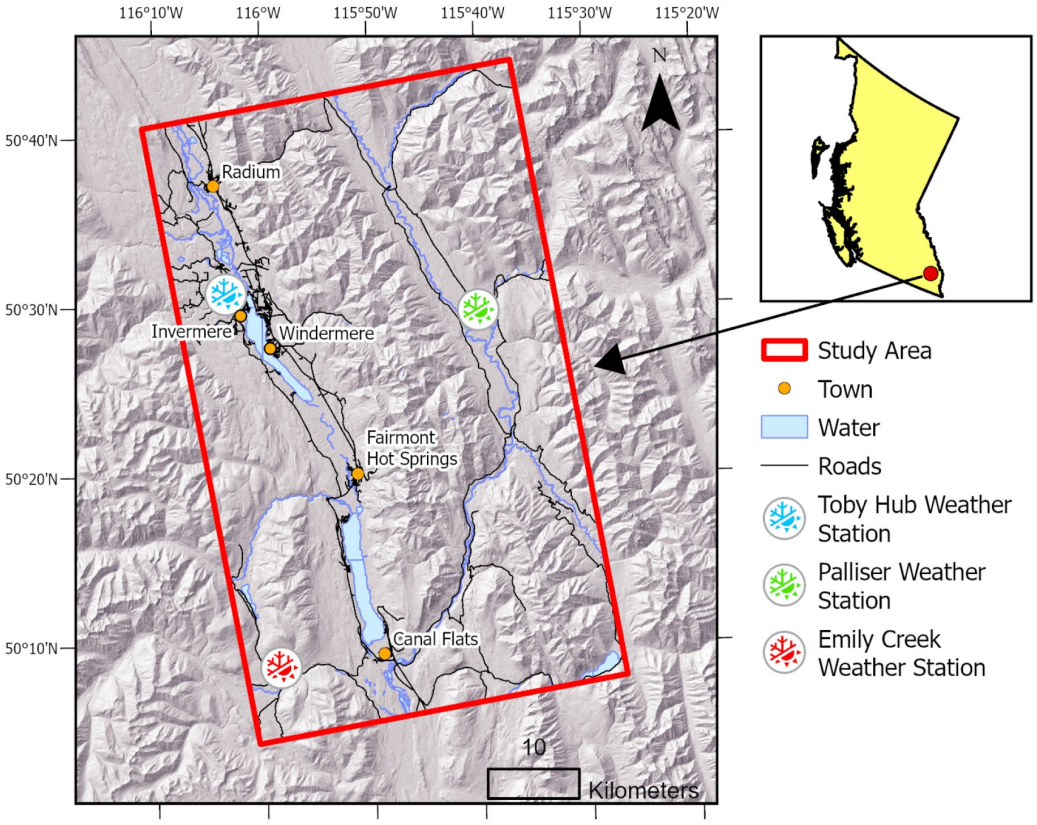


Figure 1. Study area. Red outlines the limits of the area corresponding to the ALOS-2 PALSAR-2 imagery. Three BC Wildfire Service weather stations: Toby Hub (blue), Palliser (green), and Emily Creek (red) are located within the study area.

2.2. SAR and Weather Station Data

The Japanese Aerospace Exploration Agency (JAXA) acquired repeat SAR images throughout the 2023 fire season at fourteen-day increments from 14 April to 27 October using the L-band ALOS-2 PALSAR-2 system. Each image was acquired in the morning at 07:30 local time in the high-sensitive fully polarimetric (HBQ) mode of acquisition in ascending passes and right-looking configuration. The nominal incidence angles ranged from 37.6° to 40.3°, with a range spacing of 2.86 m and azimuth spacing of 3.10 m.

Hourly observations of precipitation, temperature, wind, and relative humidity were collected at the Toby Hub, Palliser, and Emily Creek BC Wildfire Service weather stations. Values of FWI indices, including DC, DMC, FFMC, BUI, and ISI, were calculated daily at 12:00. Fourteen images were associated with 12:00 h DC and DMC values from each of the three weather stations on each image date. The Palliser weather station did not collect data from 19 May to 30 May, and the ALOS-2 PALSAR-2 image from this period (26 May) was not used to maintain an equal sample size among weather stations.

2.3. Model Variables

The polarimetric variables derived from terrain-corrected L-band imagery that were selected for use in this study are listed in Table 1. The selected variables were previously observed to have both statistically significant differences according to a one-way analysis of variance and distinguishable differences according to an analysis of normalized differences between two varying DC states [31]. The parameters of the Cloude–Pottier Decomposition are the exception to this. Although not sensitive to DC [31], these parameters describe scattering structure [36,38] and may help partition moisture effects from structural effects of vegetation in the regression models [39].

Table 1. Polarimetric variables used as model inputs, including abbreviations. Sensitivities determined according to Loncar et al. [31].

Variable Type	Variable	Abbreviation	Sensitivity
Backscatter (terrain-flattened γ^o)	L-HH	L-HH	Moisture
	L-HV	L-HV	
	L-VV	L-VV	
Van Zyl Decomposition	Double-bounce scattering	VZ-dbl	Moisture
	Surface scattering	VZ-srf	
	Volume scattering	VZ-vol	
Cloude–Pottier Decomposition	Entropy	CP-H	Fuel type
	Anisotropy	CP-A	
	alpha angle	CP-α	
Polarimetric discriminator	Maximum of the completely polarized component	Pol-max	Moisture
	Minimum of the completely polarized component	Pol-min	Moisture
	Maximum of the completely unpolarized component	UnPol-max	Moisture
	Maximum of the received power	Pr-max	Moisture
	Maximum of the scattered intensity	S-max	Moisture
	Minimum of the scattered intensity	S-min	Moisture

An additional variable, day of year (DOY), was included in the study. The DOY accounts for seasonal changes in vegetation [40] and, more importantly, patterns of increasing DC that predictably occur throughout the fire season [41]. Low DC values occur in the spring from the saturation of deep soil and heavy fuels following snowmelt. The accumulation of drying days throughout the summer increases the DC. The reduction in day length in autumn usually results in a decline in or maintenance of the DC [42]. Figure 2 uses 10-year DC data from the Toby Hub, Palliser, and Emily Creek weather stations to confirm that the previously described patterns predictably occur in the study area.

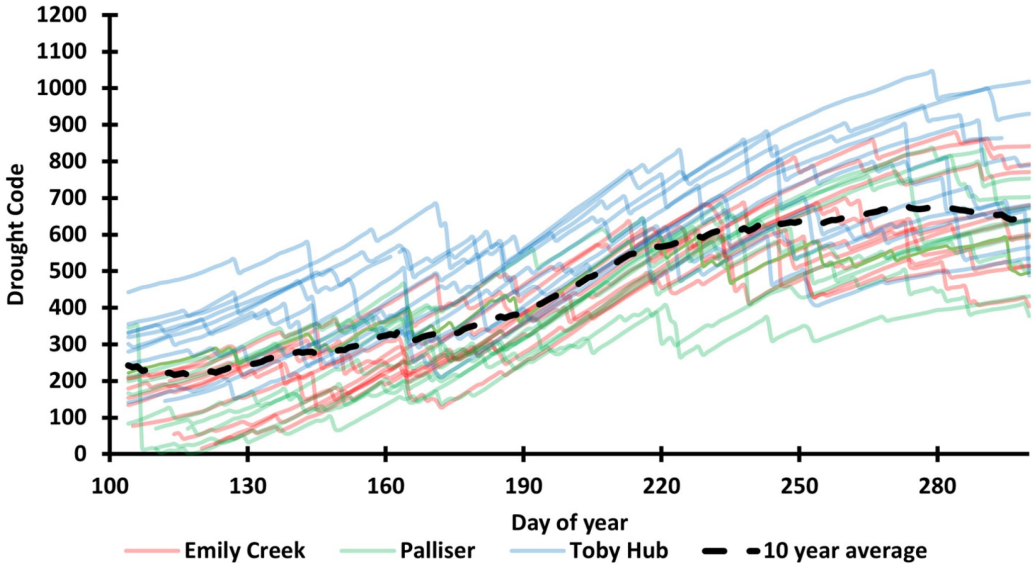


Figure 2. Ten-year (2014 to 2023) Drought Code values for the Emily Creek, Palliser, and Toby Hub weather stations by day of year and the average.

2.4. Image Processing

Figure 3 describes the general methodology used in the study. Level 1.1 single-look complex ALOS-2 PALSAR-2 imagery in CEOS format was processed according to Loncar et al. [31] using the European Space Agency's Sentinel Application Platform (SNAP) 12.0. Images were converted from Digital Numbers to sigma nought (σ^o) [43] and a Faraday rotation correction was applied [44]. Speckle was reduced using a 5 × 5 Refined Sigma Lee filter [45]. Data were converted from a scattering matrix into a coherency matrix. The terrain flattening algorithm of Small [27] normalized the coherency matrix into terrain-flattened γ^o using a 12.5 m ALOS PALSAR-derived DEM from the Alaska Satellite Facility. POA compensation was performed using the circular-polarization method [28,29].

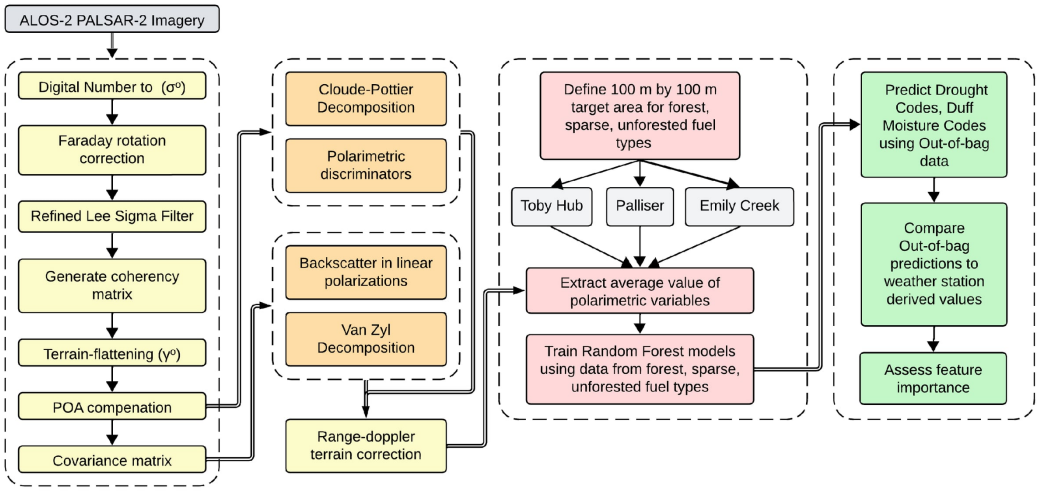


Figure 3. Workflow of ALOS-2 PALSAR-2 imagery processing, generation of polarimetric variables, random forest modelling, and model evaluation.

From the coherency matrix, the parameters of the Cloude–Pottier Decomposition and a covariance matrix were calculated. From the covariance matrix, terrain-flattened γ^o backscatter in HH, HV, and VV polarizations was extracted, and the parameters of the Van Zyl Decomposition were determined. Polarimetric discriminators (S-max, S-min,

Pr-max, Pol-max, Pol-min, UnPol-max) were calculated from the coherency matrix using the PSPOLDIS algorithm in PCI Geomatics Catalyst Professional 3.0.3. All polarimetric variables were geometrically terrain-corrected using the Range Doppler method [30] and geocoded into the Universal Transverse Mercator (UTM) Zone 11N projection using SNAP.

2.5. Model Development

The values of each polarimetric variable were extracted from 100 m by 100 m target areas comprising approximately 484 image pixels at a 4.5 m by 4.5 m ground resolution using ESRI ArcGIS Pro 3.7. This size allows for a large window necessary to reduce the influence of speckle. For each target area, the average value of each polarimetric variable was calculated and used as model input. For each weather station, three 100 m × 100 m homogeneous target areas were selected: one forested, one sparse, and one unforested using high-resolution optical imagery. All target areas were located within the immediate 1 km^2 footprints of weather stations to ensure that all polarimetric data extracted from the target areas are spatially representative of the conditions observed at the weather stations.

Random forest (RF) regression models were developed using the Random-Forest package (version 4.7-1.2) [46] for RStudio 2023.09.1. RF regression is a machine-learning method that uses multiple decision trees, each comprising random subsets of the dataset, to predict the average target value of all the trees [47]. The RF regression method has been shown to be robust and well-suited because of its ability to address non-linear relationships between polarimetric variables and moisture amid confounding effects such as those from terrain and vegetation [48,49]. A unique RF model was developed for each of the three fuel types to account for structural differences between the fuel types, which can significantly affect the polarimetric data [50]. Each model was trained using the average values of the polarimetric variables listed in Table 1 that were extracted from each station's target areas as inputs. The number of trees was set to 1000 (the number of trees was tested in increments of 100, and negligible improvement to model performance occurred beyond 1000 trees). A total of 15 variables were tried at each split (the number of variables tried at each split was tested from 5 to 15, and best model performance occurred at 15 variables). Training data for each model comprised one sample site per each of the three weather stations across fourteen images, resulting in N = 42 samples per model. The sample size was limited to 42 due to the availability of ALOS-2 PALSAR-2 images (14 images multiplied by 3 weather stations).

Models predicted (1) DC using only SAR data derived from ALOS-2 PALSAR-2 imagery, then (2) DC using SAR + DOY data. The predictive power of DOY was quantified by modelling (3) DC using only DOY. Finally, (4) the DMC was predicted using only SAR data. The DOY was not used in the DMC prediction models because the DMC does not follow a seasonal pattern like the DC.

2.6. Model Analysis

The small sample sizes did not allow for the dataset to be separated into training and validation sets. The out-of-bag (OOB) evaluation method was employed to assess model-predicted values against those derived by the weather stations. In the RF model, each tree is trained using only a random portion of the data. The OOB method predicts DC and DMC using only data that was not used to train each tree [47]. The OOB predictions provide estimates of model performance with unseen data and are especially useful when sample sizes are small. OOB predictions for all 42 samples for each model were compared to actual weather station-derived DC and DMC values. Each RF model was run 10 times, and DC and DMC predictions were averaged across iterations to reduce model-to-model variability.

The proportion of variation explained by each model was assessed using the coefficient of determination (R^2). Model prediction errors were assessed using the root mean square error (RMSE). The importance of each input variable in the models was evaluated using the percentage increase in mean square error (% Inc MSE) metric, which describes the average increase in squared residuals of the randomly permuted variables. Correlations between model variables were evaluated according to each fuel type using Pearson's correlation coefficient [51].

For DC models, the incremental value of SAR data over DOY was compared by fuel type using the difference in RMSE (ΔRMSE) between the model trained using DOY and the model trained using SAR + DOY. A residual analysis assessed whether SAR data explained variation in DC that is not captured by DOY. DOY model residual values were calculated as the differences between weather station-derived DC values and OOB predicted DC values. Residual values were modelled using SAR data for each fuel type. As with the previous RF models, residual models were run 10 times, and OOB predictions were averaged across iterations. Model performance was assessed using the R^2 and RMSE between observed DOY residual values and OOB-predicted residual values.

The ability of the models to spatially generalize fuel moisture beyond the weather stations was assessed using leave-one-station-out (LOSO) validation. Across three folds, DC and DMC models were trained for each fuel type using data from two stations (N = 28) and independently validated using data from the remaining station (N = 14). Each RF model was run 10 times, and predictions were averaged across iterations to reduce between-model variability. The values of the RMSE evaluated the prediction accuracy of each held-out station.

3. Results

3.1. Fuel Moisture Code Observations

DC (Figure 4) and DMC (Figure 5) values were compared to each ALOS-2 PALSAR-2 image. Different DC values were observed at the three weather stations despite them only being located between 27 and 44 km from one another. Spring differences in DC resulted from disparities in overwintering precipitation [8], with the Toby Hub weather station having much higher startup values than the Palliser and Emily Creek stations. The DC values at all three stations decreased between 9 June and 23 June due to a significant rainfall event followed by a drying trend that generally increased the DC for the remainder of the fire season. The DMC was more inconsistent from day to day than the DC and did not follow a seasonal pattern. Periods of increasing DMC indicate drying trends, whereas decreases in DMC generally follow precipitation events. Differences in DMC values between weather stations are likely to result from uneven precipitation patterns that tend to occur in mountainous regions [52].

3.2. Predicted Versus Actual Drought Codes

The OOB-predicted DC values for each sample site were compared to actual DC values from each associated weather station (Figure 6). Models trained using only SAR data were evaluated first. The model that used data from sparse sites (Figure 6B) had a higher R^2 value (0.49 ± 0.01) and lower RMSE (165.65 ± 0.47) than the model that used data from forest sites (Figure 6A, $R^2 = 0.39 \pm 0.01$, RMSE = 173.80 ± 1.06). The model using data from unforested sites (Figure 6C) had a considerably lower R^2 at 0.15 ± 0.01 and a higher RMSE of 205.96 ± 1.16. Models trained using SAR + DOY data had higher R^2 values and lower RMSE values in forest (Figure 6D, $R^2 = 0.88 \pm 0.00$, RMSE = 78.42 ± 0.27), sparse (Figure 6E, $R^2 = 0.94 \pm 0.00$, RMSE = 52.35 ± 0.51), and unforested (Figure 6F, $R^2 = 0.92 \pm 0.01$, RMSE = 63.76 ± 0.61) sites relative to those trained using only SAR data. The model that

was trained using only DOY (Figure 6G) had a relatively high R^2 (0.86 ± 0.00) and low RMSE (83.21 ± 0.42). All models that included SAR + DOY data reduced the overall OOB error relative to the DOY-only model. RMSE values for the SAR + DOY model decreased in forest (ΔRMSE = 4.79 ± 0.69), sparse (ΔRMSE = 30.86 ± 0.93), and unforested (ΔRMSE = 19.45 ± 1.03) sites relative to the DOY model (Table 2).

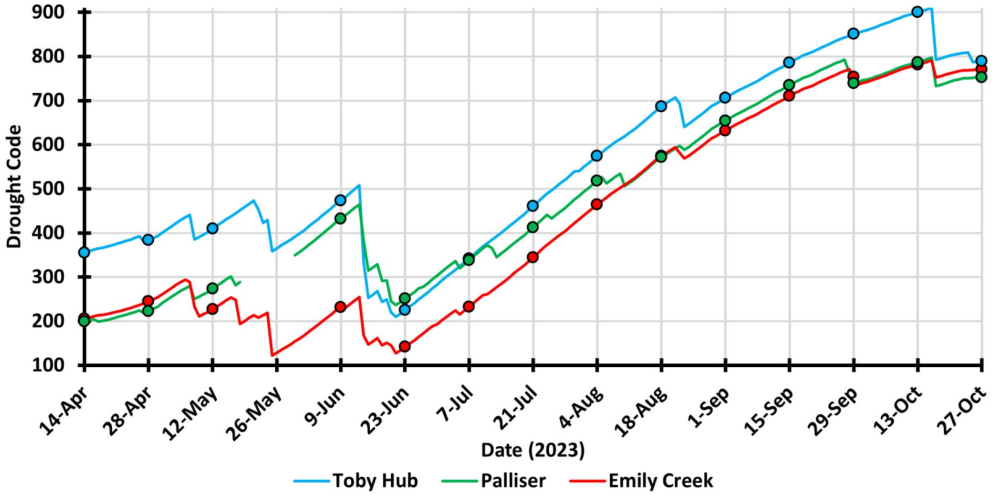


Figure 4. Drought Code values from the Toby Hub, Palliser, and Emily Creek BC Wildfire Service weather stations throughout the 2023 fire season. Lines represent daily 12:00 observations; points represent Drought Code values on the ALOS-2 PALSAR-2 image acquisition dates. Some data points are unavailable for the Palliser weather station.

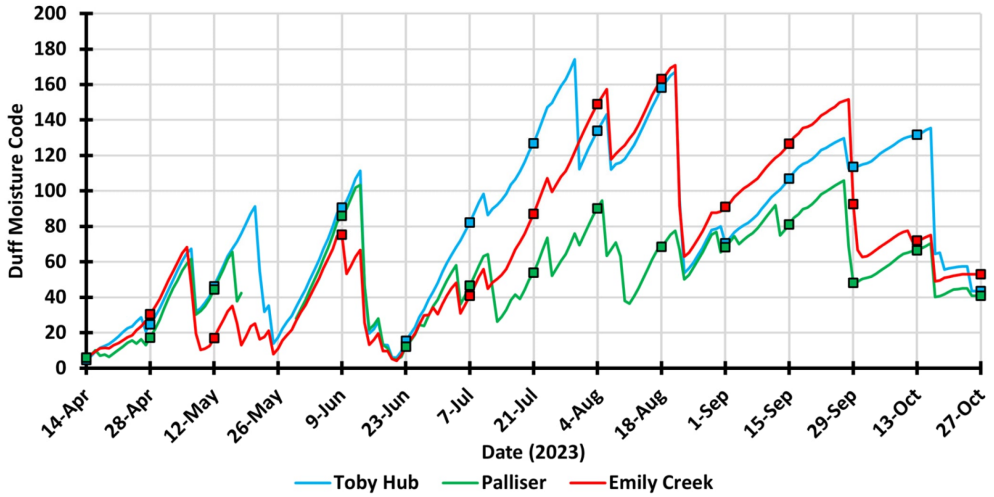


Figure 5. Duff Moisture Code values from the Toby Hub, Palliser, and Emily Creek BC Wildfire Service weather stations throughout the 2023 fire season. Lines represent daily 12:00 observations; squares represent Duff Moisture Code values on the ALOS-2 PALSAR-2 image acquisition dates. Some data are unavailable for the Palliser weather station.

Table 2. Root mean square error (RMSE) in day of year (DOY) model and SAR + day of year (SAR + DOY) models. Differences in RMSE (ΔRMSE) are calculated as RMSE (DOY)–RMSE (SAR + DOY).

Fuel Type	RMSE (DOY)	RMSE (SAR + DOY)	ΔRMSE
Forest	83.21 ± 0.42	78.42 ± 0.27	4.79 ± 0.69
Sparse	83.21 ± 0.42	52.35 ± 0.51	30.86 ± 0.93
Unforested	83.21 ± 0.42	63.76 ± 0.61	19.45 ± 1.03

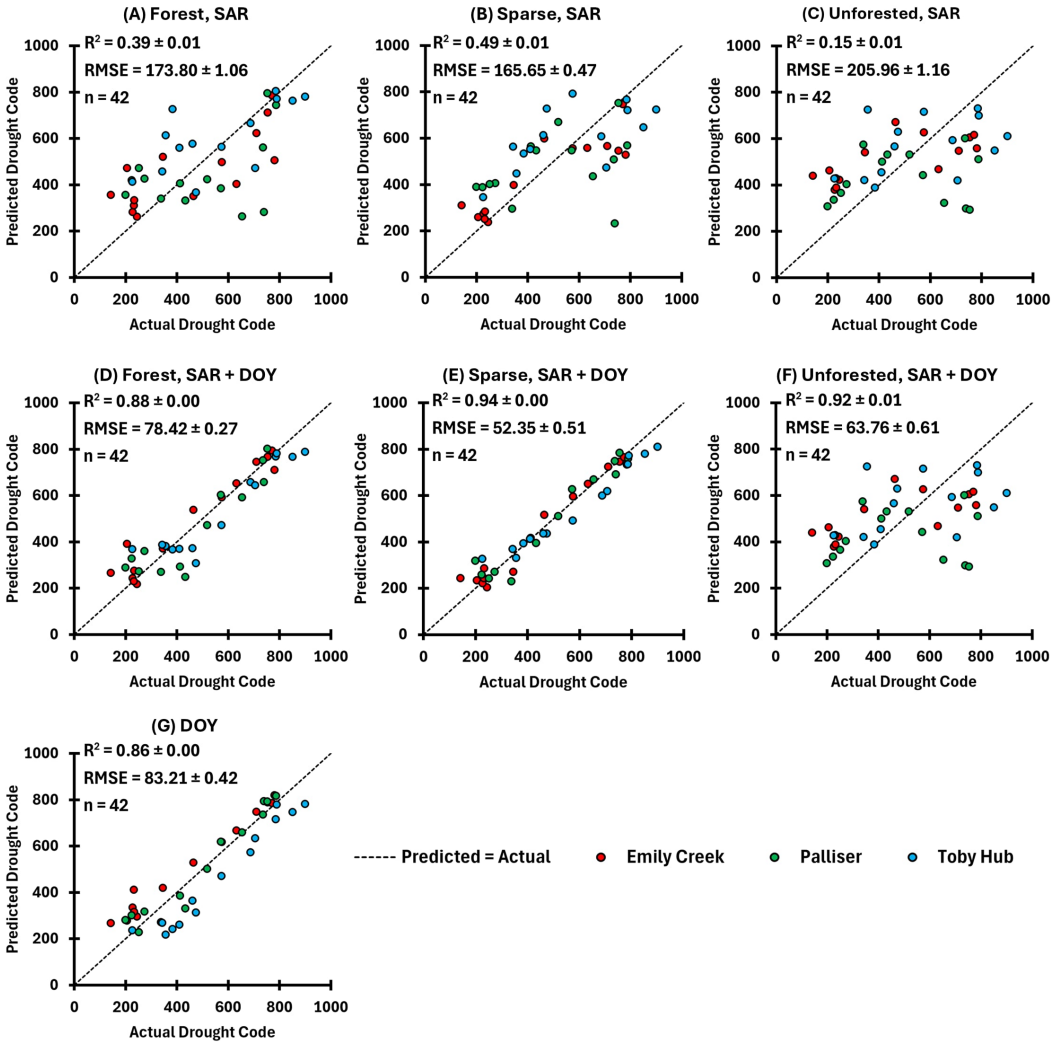


Figure 6. Out-of-bag predicted Drought Codes versus actual weather station-derived Drought Codes stratified according to weather station. Each predicted value represents the average out-of-bag prediction from 10 random forest model iterations. Models use only SAR data from (**A**) forest, (**B**) sparse, and (**C**) unforested sites. Models use SAR data and day of year from (**D**) forest, (**E**) sparse, and (**F**) unforested sites. Model (**G**) uses only day of year.

Residual errors in DC from the DOY model were modelled using SAR data (Table 3). The model that used data from sparse sites explained 55% of the residual variation and reduced the RMSE by 27.73 ± 0.86. The model that used data from unforested sites explained 43% of the variation and reduced the RMSE by 20.61 ± 0.82. Only 16% of the variation was explained by the model trained using forest data, which reduced the RMSE by 7.17 ± 1.06.

Table 3. Random forest models of DOY residuals predicted using SAR data. Residuals were calculated as actual weather station-derived Drought Code minus OOB-predicted Drought Code from the DOY-only model.

Fuel Type	RMSE (DOY)	Residual R^2 (SAR)	Residual RMSE (SAR)	ΔRMSE
Forest	83.21 ± 0.42	0.16 ± 0.01	76.04 ± 0.64	7.17 ± 1.06
Sparse	83.21 ± 0.42	0.55 ± 0.01	55.48 ± 0.44	27.73 ± 0.86
Unforested	83.21 ± 0.42	0.43 ± 0.01	62.60 ± 0.40	20.61 ± 0.82

The ability to spatially generalize the DC beyond the training weather stations was evaluated using LOSO analysis (Table 4). Models trained using SAR data had higher RMSE values than those trained using DOY or SAR + DOY data across all weather stations and fuel types. DOY + SAR models had lower errors than DOY models in five of the nine sites, including sparse fuel types for all weather stations, and all fuel types for the Toby Hub weather station. DOY models had lower error than DOY + SAR models for all forest and unforested sites at the Emily Creek and Palliser weather stations. RMSE values calculated during the LOSO analysis were generally higher than OOB predicted RMSE values except for the Emily Creek–sparse and Palliser–sparse pairs.

Table 4. Leave-one-station-out analysis for Drought Code prediction models trained using DOY, SAR, and SAR + DOY. RMSEs are compared for the weather station that was excluded during model training.

Weather Station	Fuel Type	RMSE (DOY)	RMSE (SAR)	RMSE (SAR + DOY)
Emily Creek	Forest	69.54 ± 0.50	215.70 ± 2.06	100.02 ± 1.50
	Sparse	69.54 ± 0.50	216.32 ± 2.03	50.61 ± 0.73
	Unforested	69.54 ± 0.50	292.89 ± 1.41	79.66 ± 0.91
Palliser	Forest	72.08 ± 0.31	210.54 ± 1.06	87.32 ± 0.83
	Sparse	72.08 ± 0.31	183.80 ± 1.16	50.88 ± 0.81
	Unforested	72.08 ± 0.31	355.77 ± 1.03	116.21 ± 1.92
Toby Hub	Forest	125.30 ± 0.39	199.21 ± 1.17	80.47 ± 1.79
	Sparse	125.30 ± 0.39	233.96 ± 1.33	71.96 ±0.75
	Unforested	125.30 ± 0.39	248.09 ± 2.05	104.69 ± 1.12

The OOB-predicted DC values were plotted against weather station-derived DC values throughout the 2023 fire season to assess the uncertainty on each image date and identify temporal patterns (Figure 7). The models trained using only SAR data (Figure 7A–C) overestimated the DC in the early (April to May) and mid (23 June to 4 August) seasons while underestimating the DC in the late season (18 August to 13 October). Models trained using SAR + DOY (Figure 7D–F) reduced the early season overestimation of DC values. Predicted DC values accurately modelled the mid- to late-season increase observed by the weather stations, regardless of fuel type. The underestimation of late-season DC was reduced for all fuel types. SAR + DOY models using data from forest and sparse sites correctly predicted the Toby Hub station to have higher DC values than the seasonal average for much of the fire season. Similarly, the Emily Creek station was predicted to have a lower DC than the seasonal average for much of the fire season using data from forest and sparse sites. The model trained using only DOY predicted only seasonal averages and did not deviate from the average combined DC of the three weather stations.

3.3. Predicted Versus Actual Duff Moisture Codes

The OOB predicted DMC values for each sample site were compared to actual DMC values from each associated weather station (Figure 8). The model trained using data from sparse sites (Figure 8B) had the highest R^2 value of 0.64 ± 0.00 and the lowest RMSE at 26.07 ± 0.18. The model that used data from unforested sites (Figure 8C) had a lower R^2 value of 0.47 ± 0.01 and a higher RMSE of 31.52 ± 0.18. The lowest R^2 value of 0.12 ± 0.01 and the highest RMSE of 40.71 ± 0.27 resulted from the model using data from forest sites (Figure 8A).

The ability to spatially generalize the DMC beyond the training weather stations was evaluated using LOSO analysis (Table 5). All weather stations and fuel type pairs except for Palliser–forest had higher RMSE values than those obtained from the OOB validation.

The Palliser weather station had a lower LOSO DMC error than Emily Creek or Toby Hub across all fuel types.

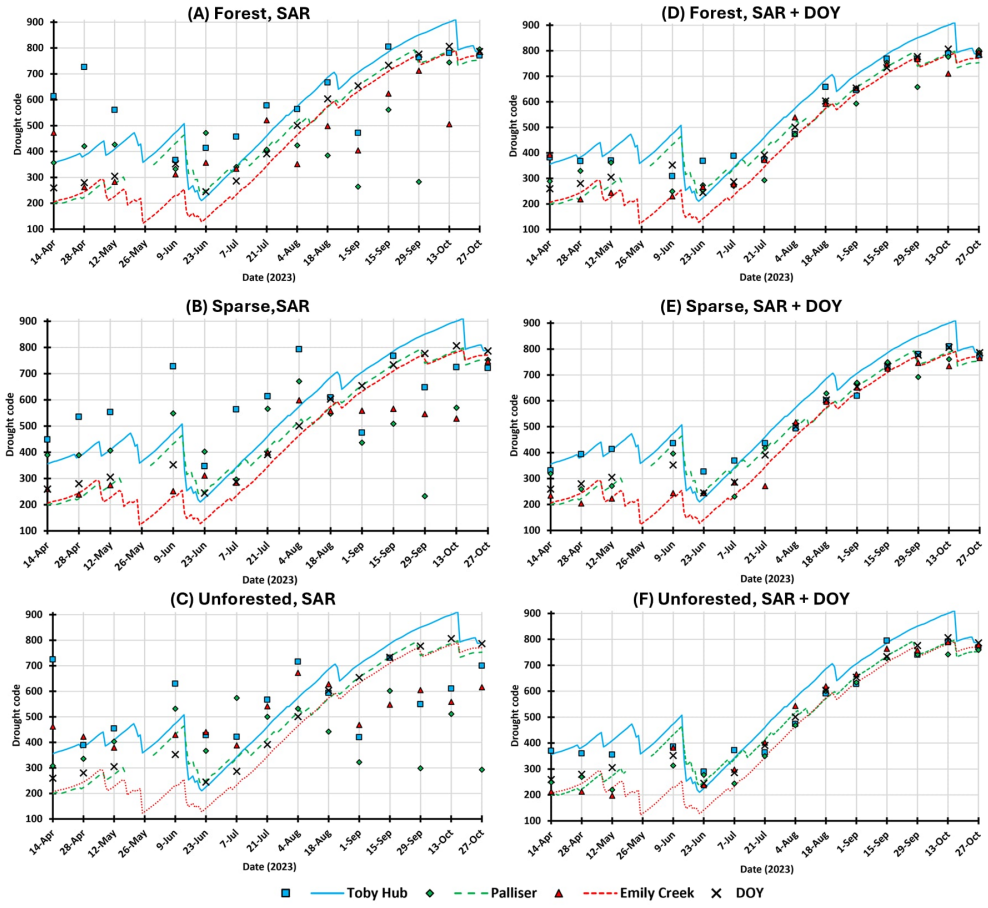


Figure 7. Actual weather station-derived Drought Codes (lines) from the Toby Hub (blue), Palliser (green), and Emily Creek (red) BC Wildfire Service weather stations versus out-of-bag predicted Drought Codes for Toby Hub (blue squares), Palliser (green diamonds), and Emily Creek (red triangles). Each predicted value represents the average out-of-bag prediction from 10 random forest model iterations. Models were developed using SAR data from (**A**) forested, (**B**) sparse, and (**C**) unforested sites. Models were developed using SAR data and day of year from (**D**) forest, (**E**) sparse, and (**F**) unforested sites. Out-of-bag predicted drought code values (black X) from models using only the day of year are included in each figure.

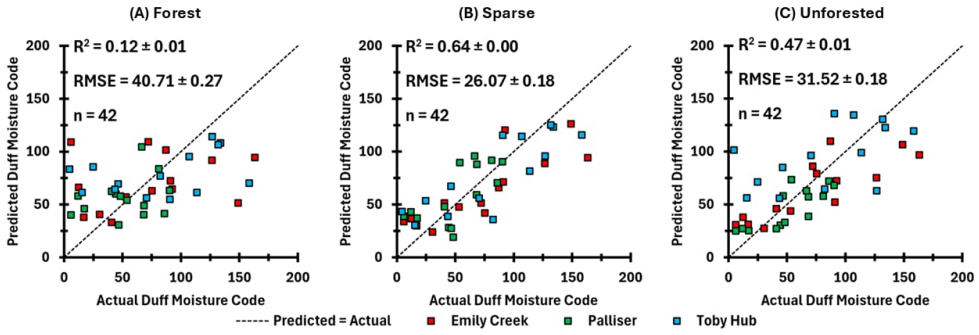


Figure 8. Out-of-bag predicted Duff Moisture Codes versus actual weather station-derived Duff Moisture Code values stratified according to weather station. Each predicted value represents the average out-of-bag prediction from 10 random forest model iterations. Models use data from (**A**) forest, (**B**) sparse, and (**C**) unforested sites.

Table 5. Leave-one-station-out analysis for Duff Moisture Code prediction models trained using SAR data. RMSEs are compared for the weather station that was excluded during model training.

Weather Station	RMSE (Forest)	RMSE (Sparse)	RMSE (Unforested)
Emily Creek	44.65 ± 0.27	42.35 ± 0.33	41.63 ± 0.41
Palliser	31.30 ± 0.42	32.08 ± 0.26	37.00 ± 0.29
Toby Hub	45.74 ± 0.28	43.46 ± 0.24	44.16 ± 0.35

The OOB predicted DMC values were plotted against weather station-derived DMC values throughout the 2023 fire season (Figure 9). The DMC values that were predicted using the model that was trained using data from forest sites (Figure 9A) had little variation between the image dates. Higher DMC values, such as on 9 June, 4 August, and 18 August, were underestimated, while very low DMC values, such as on Apr. 14 and Jun. 23, were overestimated. The model trained using data from sparse sites (Figure 9B) reduced the underestimation of high DMC values and the overestimation of low DMC dates in comparison to the forest model. However, the lowest DMC conditions on 14 April and 23 June were overestimated to a large degree, and an exceptionally large outlier occurred with the Toby Hub weather station on 29 September. The model trained using data from unforested sites (Figure 9C) predicted DMC values with less difference to weather station values than the forested sites, but slightly more than the model trained using data from the sparse sites.

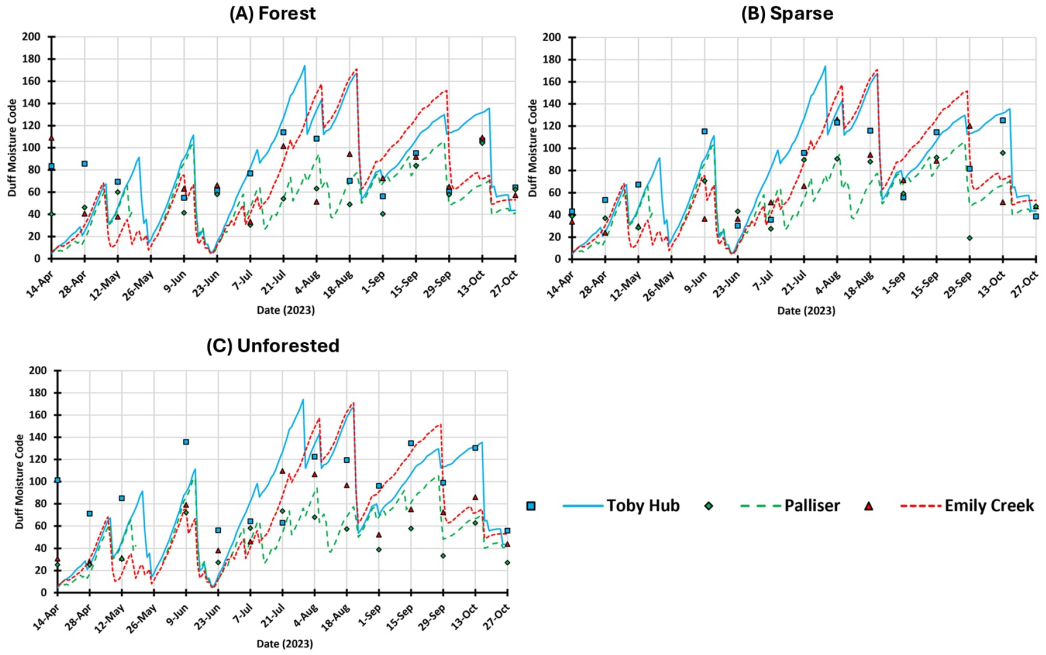


Figure 9. Actual weather station-derived Duff Moisture Codes (lines) from the Toby Hub (blue), Palliser (green), and Emily Creek (red) BC Wildfire Service weather stations versus out-of-bag predicted Duff Moisture Code values for Toby Hub (blue squares), Palliser (green diamonds), and Emily Creek (red triangles). from models developed using polarimetric data from (**A**) forested, (**B**) sparse, and (**C**) unforested sites.

3.4. Model Feature Selection

The % Inc MSE assessed the importance of each input variable to the DC prediction models (Figure 10). Models trained using only SAR data were evaluated first. The model trained using data from forest sites (Figure 10A) had VZ-dbl and L-VV as the most important variables. Each increased the MSE by more than 15%. Pol-min was the most important

variable in the models trained using data from sparse sites (Figure 10B), increasing the MSE by more than 15%. A cluster of seven variables (S-max, VZ-srf, Pol-max, L-HH, Pr-max, CP-H, L-VV) increased the MSE by 7% to 12%. For the unforested model (Figure 10C), CP-α was the most important variable, and the only variable to exceed a 15% increase in MSE. Then, models trained to predict the DC using SAR + DOY were assessed. DOY was by far the most important variable regardless of fuel type, increasing the MSE by 79% to 87%. L-VV remained the most important polarimetric variable in the model trained using data from forest sites (Figure 10D), but the importance of VZ-dbl decreased. CP-H became the most important polarimetric variable in the model trained using data from sparse sites (Figure 10E), and CP-A for the model trained using data from unforested sites (Figure 10F).

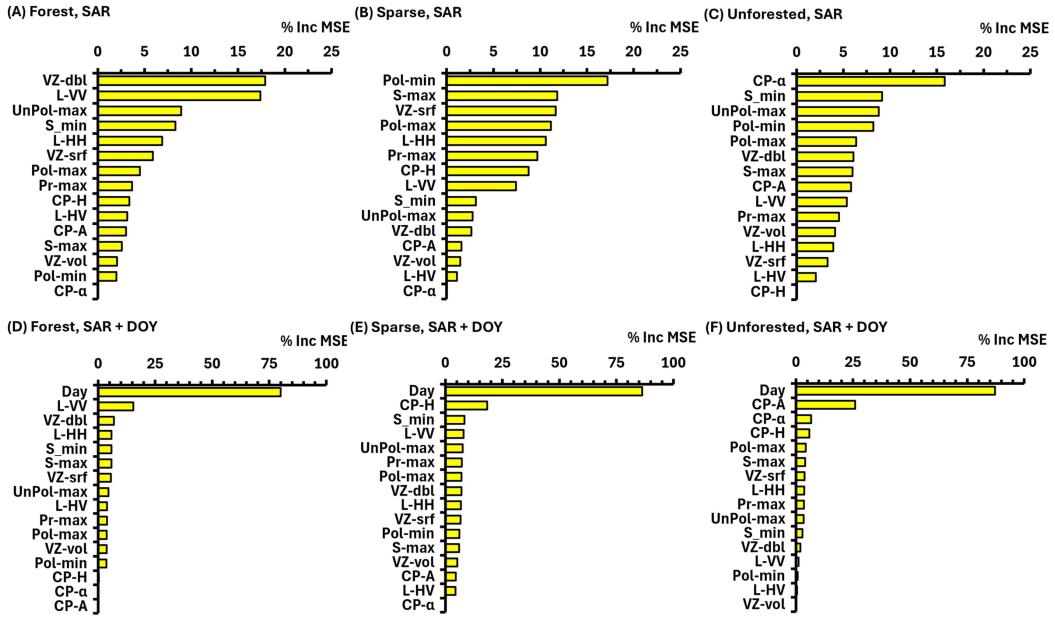


Figure 10. Average percentage increase in mean square error for each input variable in the Drought Code prediction models across 10 random forest model iterations. Models use SAR data from (**A**) forest, (**B**) sparse, and (**C**) unforested sites. Models use SAR data and day of year from (**D**) forest, (**E**) sparse, and (**F**) unforested sites.

The importance of each variable to the DMC prediction models was evaluated in Figure 11 using the % Inc MSE. The most important variables to the model trained using data from forested (Figure 11A) sites were L-VV, S-min, and VZ-dbl. Each increased the MSE by more than 10%. CP-H and CP-α were most important to the model trained using data from sparse (Figure 11B) sites, increasing the MSE by 38% and 20%, respectively. CP-A, which exceeded a 20% increase in MSE, was the most important variable to the model trained using data from unforested (Figure 11C) sites. Pol-min and VZ-dbl additionally exceeded 10% increases.

Correlations between variables were assessed according to each fuel type using Pearson's correlation coefficient (Figure 12). Backscatter, parameters of the VanZyl Decomposition, and polarimetric discriminators were highly positively correlated (Pearson's correlation coefficient > 0.8) regardless of the fuel type. Parameters of the Cloude–Pottier Decomposition were exceptions. CP-A was weakly positively correlated with other SAR variables in forested and unforested sites, but with little correlation in sparse sites. Moderate to highly positive correlations occurred between CP-α and other SAR variables in forest and sparse sites, while highly negative correlations existed in unforested sites. For CP-H, highly negative correlations occurred with other SAR variables in unforested sites. SAR variables generally had negative correlations with DMC and DC. SAR variables were more highly

correlated with DC in forest and sparse sites than in unforested sites, and more negatively correlated with DMC in sparse and unforested sites than in forested sites.

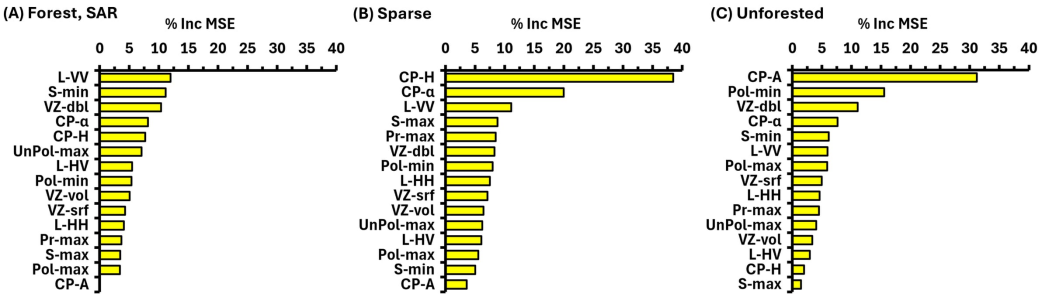


Figure 11. Average percentage increase in mean square error for each input variable in the Duff Moisture Code prediction models across 10 random forest model iterations. Models use SAR data from (**A**) forest, (**B**) sparse, and (**C**) unforested sites.

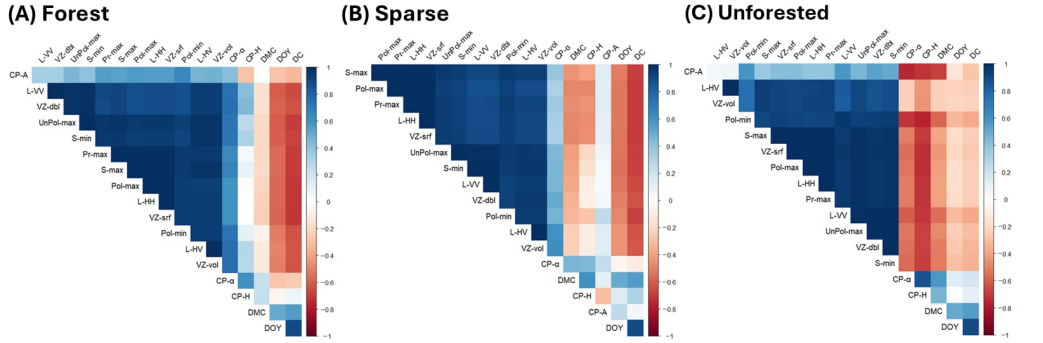


Figure 12. Pearson's correlation matrix between predictor SAR variables, DOY, and weather station-derived fuel moisture codes using data from (**A**) forest, (**B**) sparse, (**C**) unforested sites.

4. Discussion

The accuracy of the DC prediction models differed depending on the fuel type from which the SAR data were sampled. R^2 values were greatest in the model developed using SAR data from sparse sites, and slightly smaller in the model developed using data from forested sites. R^2 values were much lower in the model developed using data from unforested sites. This aligns with previous findings where polarimetric variables derived from terrain-corrected L-band imagery were more sensitive to differences in DC in forested and sparse sites than in unforested sites [31]. Because the DC is based strictly on weather observations, it cannot account for differences in moisture between different fuel types [6]. It is likely that the DC values observed by the weather stations are not representative of the moisture conditions of unforested sites, which differ in moisture-holding capacity due to differences in evapotranspiration, organic soil thickness, rainfall interception, and runoff when compared to more heavily forested sites [31]. The RF models developed using only SAR data from forested and sparse sites produced lower R^2 values than those observed by Bourgeau-Chavez et al. [22] in black spruce sites in Alaska using C-band RADARSAT-2 imagery. However, vegetation, soil, and topographic differences between flat, black spruce forests of Alaska and mountainous forests of interior BC make direct comparisons between these two studies difficult.

DOY had high predictive power and a relatively high R^2 value when it was the sole predictor variable. DOY has previously been successfully used as an input variable in fuel moisture prediction models and observed to be strongly related to the DC [53]. Environmental variables with strong relationships to the response variable, such as DOY to DC, are often more highly related to the response variables than SAR-derived variables [53–56].

However, the DOY-only model was trained and validated using only a single year of data and is limited in temporal transferability if applied to other fire seasons where differences in spring startup values, precipitation, and temperature will occur. The DOY model also only predicted the seasonal average and was unable to capture deviations in DC values higher or lower than the seasonal average.

Models trained using SAR + DOY data predicted the DC more accurately than models trained using only SAR or DOY data alone, as determined by OOB validation. The SAR + DOY model predicted deviations in DC values from the seasonal average, particularly in the case of forest and sparse sites. Analysis of residual values suggested that SAR data explains moderate error in the DOY model when using data from sparse and unforested sites, and low error when using data from forest sites. SAR variables captured additional variation associated with deviations from the seasonal DOY baseline within the sampled stations, as identified by the moderate predictive accuracy of models trained using only SAR data from forest and sparse sites. LOSO validation provided limited evidence that SAR data may spatially transfer beyond the weather stations used in model training. SAR + DOY models reduced the error in five out of nine cases when compared to DOY models on withheld weather stations. However, in four out of nine cases, the SAR + DOY models produced greater error than the DOY-only models. This suggests that relationships between SAR data and DC are site-specific to the weather stations used in model training and can be erroneous when generalized to independent locations, as determined by the higher RMSE values obtained in the LOSO models in comparison to the OOB predicted values. Each weather station from which the data were sampled from only represents a partial subset of surface conditions that occur within the study area. As a result, spatial differences across the landscape may not be accounted for during model training, and the LOSO analysis may extrapolate beyond the spatial domain of the training data.

Like DC models, the accuracy of the DMC prediction models also differed by fuel type. The model using data from sparse sites had the greatest R^2 value, whereas the model using data from unforested sites had a reduced R^2 value. The DMC model using data from the forest sites had a very low R^2 value. This suggests that DMC prediction using SAR is better suited to relatively lower biomass sites and not well suited to high-biomass forested sites. In forested sites, the depth of the duff layer (corresponding to the DMC) is highly variable at scales of a few meters because of fine-scale differences in the accumulation of litter [57]. The depth of the organic duff layer can affect the strength of the L-band backscatter by as much as 2 dB [58]. The singular DMC value that was used to train does not account for the differences in duff layer depth that affect the SAR backscatter and can overwhelm the underlying effects of moisture. No study has yet used polarimetric SAR to model the DMC. Future development of terrain-corrected L-band polarimetric SAR should prioritize DMC prediction in sparse and unforested environments, where smaller variations in fine-scale depth of the duff layer occur. Much like DC models, the LOSO analysis produced generally greater error for the DMC prediction models than the OOB analysis, suggesting that physical differences in topography, vegetation, and soil between the various sites used are not accounted for in the models.

Additional research is required to reduce the uncertainties of using terrain-corrected L-band imagery to estimate DC and DMC in mountainous and forested environments. The accuracy of the DC and DMC prediction models developed in this study is largely limited by unaccounted differences in the physical conditions of the imaged surfaces. Polarimetric data are sensitive to structural factors of a forest such as the roughness of a surface [59], the amount of biomass [60,61], tree heights [62], and the canopy density. Each of these is likely to differ between the areas from which the input data were sampled from. The three general fuel types used in this study cannot describe these differences in adequate detail. The

absence of explicit spatial information may introduce spatially varying bias when models are compared between various sites and applied across a heterogeneous environment. Supplementary information on surface structures such as lidar-derived surface roughness [63], biomass [64], forest height [65], and canopy density [66] may explain variations in the data and account for differences between sites. This information can also be related to structure-sensitive variables such as parameters of the Cloude–Pottier Decomposition, FP, or those related to scattering mechanisms such as backscatter or parameters of the Van Zyl Decomposition. The increasing availability of high-resolution, large-area coverage LiDAR data may provide the critical supplementary information necessary to account for surface factors to reduce structure-induced noise.

Additional errors are likely to occur from differences in moisture conditions between images and sample sites. Differences in soil type and composition may also affect soil water-holding capacity and its relationship to polarimetric variables [11]. Each DC value that was used to train the RF models is only related to the moisture content of a layer of deep soil and heavy fuels. Each DMC value that was used to train RF models is only related to the moisture content of the upper soil and medium fuels. However, polarimetric data are also affected by the surface litter moisture (related to the FFMC) [14] and live above-ground biomass [17]. Both moisture variables can be variable for any given DC and DMC value. This is particularly the case for the DC. In certain situations, for example, fine live above-ground biomass and surface litter can quickly become saturated by moisture from recent rainfall, but the DC can remain constant [8]. When wet, the moisture in these layers may affect the SAR data differently as opposed to if they were dry [67]. Differences in moisture associated with various fuel types or depths of the duff layer can be accounted for by calculating DC directly from in situ soil measurements [22] as opposed to using weather station calculated values, which do not account for differences in moisture between different fuel types. Understanding the moisture content of fine surface or live fuels may explain additional variations in the data. The synergistic incorporation of data from multispectral sensors [17,68,69] will be required to account for variations in moisture outside of DC and DMC.

The accuracy of the developed models is also limited by the small dataset and the single fire season of data used in this study. Data collection only occurred during the 2023 fire season, which was a dry season in BC that started with relatively high DC values in the spring and did not allow for the low extrema of DC values (less than 200) to be captured in the models. The single-season DOY data is vulnerable to bias if used to predict other seasons with interannual variability. Future models must be trained during wetter fire seasons using data across multiple years to reduce bias resulting from the conditions of the season that was used to train the model.

The RF regression models risk overfitting data due to the low number of training samples (N = 42 per model), high number of variables (15 to 16 depending on whether DOY was included), and high collinearity between several SAR variables. The high ratio of variables to fuel moisture observations limits confidence in the accuracy and spatial transferability of the developed models. SAR variables, including backscatter, parameters of the VanZyl Decomposition, and polarimetric discriminators, were highly positively correlated with each other and negatively correlated to DMC and DC. Parameters of the Cloude–Pottier Decomposition were the exception. Individual scattering contributions cannot be reliably ascertained due to the high collinearity between SAR variables. Instead, the observed importance of these variables can only inform the collective group contribution of these variables. More L-band imagery across additional weather stations is needed to capture greater variability in surface structure and moisture conditions. Model validation using a greater number of DC and DMC data points, including from independent weather

stations, is necessary to better assess the accuracy and spatial generalization of the developed models beyond the OOB and LOSO analyses.

5. Conclusions

This paper describes the first attempt at modelling fuel moisture codes of the CFFDRS using L-band polarimetric SAR data. The suitability of using terrain-corrected L-band SAR differs depending on the fuel moisture code being modelled and the fuel type from which data were acquired. Models using SAR variables predicted the DC in forested and sparse environments with moderate accuracy at weather stations, and low accuracy in unforested environments. DMC models differed, with moderate accuracy in sparse and unforested sites, and low accuracy in forested sites. The accuracy of DC models was improved by including DOY as a predictor variable. DOY-only models predicted DC with high accuracy but only predicted seasonal averages in the DC and did not account for spatial deviations from the average. The highest-accuracy DC predictions were achieved by SAR + DOY models. Modelling the residuals of the DOY-only model demonstrated that SAR data contained additional information not represented by DOY, suggesting that SAR data may inform spatial deviations from the seasonal average when combined with DOY.

Spatial generalization beyond the training weather stations was limited, as LOSO analyses generally produced greater error than OOB validation for both the DC and DMC. This suggests that SAR data is influenced not only by fuel moisture but also by site-specific differences in the landscape that are not accounted for in the models. Future improvements to DC and DMC modelling using L-band polarimetric SAR must incorporate larger datasets from additional weather stations, across multiple fire seasons, and must account for differences in biomass, canopy structure, surface roughness, soil properties, and fine-fuel moisture to allow application beyond the training weather stations. The work described in this paper develops an initial basis for modelling DC and DMC values and supports the feasibility of using terrain-corrected L-band imagery in mountainous and forested environments. The ability to use space-based SAR platforms to estimate fuel moisture codes is a significant step towards increasing the availability of spatially accurate fire weather data across the fire environment.

Author Contributions: Conceptualization, M.L., B.L., A.R., L.B.-C. and D.A.; methodology, M.L., B.L., A.R. and L.B.-C.; software, M.L.; validation, M.L., B.L., A.R. and L.B.-C.; formal analysis, M.L.; investigation, M.L.; resources, B.L. and A.R.; data curation, M.L. and A.R.; writing—original draft preparation, M.L.; writing—review and editing, M.L., B.L., A.R., L.B.-C. and D.A.; visualization, M.L.; supervision, B.L. and D.A.; project administration, B.L.; funding acquisition, B.L., A.R. All authors have read and agreed to the published version of the manuscript.

Funding: This research was funded by the BC Wildfire Service, Canada Wildfire, the Ontario Graduate Scholarship, and the Natural Sciences and Engineering Research Council Alliance Advantage Grant ALLRP 607870–25.

Data Availability Statement: The weather station data collected by the BC Wildfire Service is available from https://www.for.gov.bc.ca/ftp/HPR/external/!publish/BCWS_DATA_MART/, accessed on 17 September 2025. The original ALOS-2/PALSAR-2 Data Products are provided by JAXA. ©JAXA [2023]. All rights reserved.

Acknowledgments: This project was undertaken in part within the framework of the JAXA Kyoto & Carbon Initiative. Thanks to JAXA for the provision of the SAR datasets used within this study under the EORA-3 opportunity.

Conflicts of Interest: The authors declare no conflicts of interest.

Abbreviations

The following abbreviations are used in this manuscript:

BC	British Columbia
BUI	Buildup index
CFFDRS	Canadian Forest Fire Danger Rating System
CP-A	Cloude–Pottier Anisotropy
CP-α	Cloude–Pottier alpha angle
CP-H	Cloude–Pottier Entropy
DC	Drought Code
DEM	Digital elevation model
DMC	Duff Moisture Code
DOY	Day of year
FBP	Fire Behavior Prediction
FFMC	Fine Fuel Moisture Code
FOP	Fire Occurrence Prediction
FP	Fractional polarization
FWI	Fire Weather Index
ISI	Initial spread index
JAXA	Japanese Aerospace Exploration Agency
L-HH	L-band backscatter in the HH polarization
L-HV	L-band backscatter in the HV polarization
L-VV	L-band backscatter in the VV polarization
LOSO	Leave-one-station-out
OOB	Out-of-bag
POA	Polarization orientation angle
Pol-max	Maximum of the completely polarized component
Pol-min	Minimum of the completely polarized component
R^2	Coefficient of determination
RF	Random Forest
RMSE	Root mean square error
S-max	Maximum of the scattered intensity
S-min	Minimum of the scattered intensity
SAR	Synthetic aperture radar
SNAP	Sentinel Application Platform
UTM	Universal Transverse Mercator
VZ-dbl	Van Zyl double-bounce scattering
VZ-srf	Van Zyl surface scattering
VZ-vol	Van Zyl volume scattering

References

1. Stocks, B.J.; Lawson, B.D.; Alexander, M.E.; Van Wagner, C.E.; McAlpine, R.S.; Lynham, T.J.; Dubé, D.E. The Canadian Forest Fire Danger Rating System: An overview. *For. Chron*. **1989**, *65*, 450–457. [CrossRef]
2. Tymstra, C.; Stocks, B.J.; Cai, X.; Flannigan, M.D. Wildfire management in Canada: Review, challenges and opportunities. *Prog. Disaster Sci*. **2020**, *5*, 100045. [CrossRef]
3. Wotton, B.M. Interpreting and using outputs from the Canadian Forest Fire Danger Rating System in research applications. *Environ. Ecol. Stat*. **2009**, *16*, 107–131. [CrossRef]
4. Woolford, D.G.; Martell, D.L.; McFayden, C.B.; Evens, J.; Stacey, A.; Wotton, M.B.; Boychuck, D. The development and implementation of a human-caused wildland fire occurrence prediction system for the province of Ontario, Canada. *Can. J. For. Res*. **2021**, *51*, 303–325. [CrossRef]
5. Forestry Canada Fire Danger Group. *Development and Structure of the Canadian Forest Fire Behavior Prediction System*; Information Report ST-X-3; Forestry Canada, Science and Sustainable Development Directorate: Ottawa, ON, Canada, 1992; p. 64.
6. Van Wagner, C.E. *Development and Structure of the Canadian Forest Fire Weather Index System*; Forestry Technical Report 35; Canadian Forestry Service: Ottawa, ON, Canada, 1987; p. 37.
7. Van Wagner, C.E. Modelling logic and the Canadian Forest Fire Behavior Prediction System. *For. Chron*. **1998**, *74*, 50–52. [CrossRef]

8. Lawson, B.D.; Armitage, O.B. *Weather Guide for the Canadian Forest Fire Danger Rating System*; Canadian Forest Service, Northern Forestry Centre: Edmonton, AB, Canada, 2008; p. 84.
9. Flannigan, M.D.; Wotton, B.M. A study of interpolation methods for forest fire danger rating in Canada. *Can. J. For. Res.* **1989**, *19*, 1059–1066. [CrossRef]
10. Leblon, B. Monitoring forest fire danger with remote sensing. *Nat. Hazards* **2005**, *35*, 343–359. [CrossRef]
11. Cihlar, J.; Ulaby, F.T. *Dielectric Properties of Soils as a Function of Moisture Content*; CRES Technical Report 177-47; The University of Kansas Center for Research: Lawrence, KS, USA, 1974; p. 61.
12. Abbott, K.N.; Leblon, B.; Staples, G.C.; Maclean, D.A.; Alexander, M.E. Fire danger monitoring using RADARSAT-1 over northern boreal forests. *Int. J. Remote Sens.* **2007**, *28*, 1317–1338. [CrossRef]
13. Bourgeau-Chavez, L.L.; Kasischke, E.S.; Rutherford, M.D. Evaluation of ERS SAR data for prediction of fire danger in a boreal region. *Int. J. Wildland Fire* **1999**, *9*, 183–194. [CrossRef]
14. Leblon, B.; Kasischke, E.; Alexander, M.; Doyle, M.; Abbott, M. Fire danger monitoring using ERS-1 SAR images in the case of northern boreal forests. *Nat. Hazards* **2002**, *27*, 231–255. [CrossRef]
15. Oldak, A.; Jackson, T.J.; Starks, P.; Elliott, R. Mapping near-surface soil moisture on regional scale using ERS-2 SAR data. *Int. J. Remote Sens.* **2003**, *24*, 4579–4598. [CrossRef]
16. Karthikeyan, L.; Pan, M.; Wanders, N.; Kumar, D.N.; Wood, E.F. Four decades of microwave satellite soil moisture observations: Part 1. A review of retrieval algorithms. *Adv. Water Resour.* **2017**, *109*, 106–120. [CrossRef]
17. Rao, K.; Williams, A.P.; Flefil, J.F.; Konings, A.G. SAR-enhanced mapping of live fuel moisture content. *Remote Sens. Environ.* **2020**, *245*, 111797. [CrossRef]
18. Tanase, M.A.; Panciera, R.; Lowell, K.; Aponte, C. Monitoring live fuel moisture in semiarid environments using L-band radar data. *Int. J. Wildland Fire* **2015**, *24*, 560–572. [CrossRef]
19. Freeman, A.; Durden, S.L. A three-component scattering model for polarimetric SAR data. *IEEE Trans. Geosci. Remote Sens.* **1998**, *36*, 963–973. [CrossRef]
20. Van Zyl, J.J.; Arii, M.; Kim, Y. Model-based decomposition of polarimetric SAR covariance matrices constrained for nonnegative eigenvalues. *IEEE Trans. Geosci. Remote Sens.* **2011**, *49*, 3452–3459. [CrossRef]
21. Bourgeau-Chavez, L.L.; Leblon, B.; Charbonneau, F.; Buckley, J.R. Assessment of polarimetric SAR data for discrimination between wet versus dry soil moisture conditions. *Int. J. Remote Sens.* **2013**, *34*, 709–730. [CrossRef]
22. Bourgeau-Chavez, L.L.; Leblon, B.; Charbonneau, F.; Buckley, J.R. Evaluation of polarimetric Radarsat-2 SAR data for development of soil moisture retrieval algorithms over a chronosequence of black spruce boreal forests. *Remote Sens. Environ.* **2013**, *132*, 71–85. [CrossRef]
23. Magagi, R.; Jammali, S.; Goïta, G.; Wang, H.; Colliander, A. Potential of L- and C-bands polarimetric SAR data for monitoring soil moisture over forested sites. *Remote Sens.* **2022**, *14*, 5317. [CrossRef]
24. Small, D.; Zuberbühler, L.; Shubert, A.; Meier, E. Terrain-flattened gamma nought Radarsat-2 backscatter. *Can. J. Remote Sens.* **2011**, *7*, 493–499. [CrossRef]
25. Wang, P.; Ma, Q.; Wang, J.; Hong, W.; Li, Y.; Chen, Z. An improved SAR radiometric terrain correction method and its application in polarimetric SAR terrain effect reduction. *Prog. Electromagn. Res. B* **2013**, *54*, 107–128. [CrossRef]
26. Atwood, D.K.; Small, D.; Gens, R. Improved PolSAR land classification with radiometric correction of the coherency matrix. *IEEE J. Sel. Top. Appl. Earth Obs. Remote Sens.* **2012**, *5*, 848–856. [CrossRef]
27. Small, D. Flattening gamma: Radiometric terrain correction for SAR imagery. *IEEE Trans. Geosci. Remote Sens.* **2011**, *49*, 3081–3093. [CrossRef]
28. Lee, J.-S.; Schuler, D.L.; Ainsworth, T.L. Polarimetric data compensation for terrain azimuth slope variation. *IEEE Trans. Geosci. Remote Sens.* **2000**, *38*, 2153–2163. [CrossRef]
29. Lee, J.-S.; Schuler, D.L.; Ainsworth, T.L.; Krogager, E.; Kasilingam, D.; Boerner, W.-M. On the estimation of radar polarization orientation shifts induced by terrain slopes. *IEEE Trans. Geosci. Remote Sens.* **2002**, *40*, 30–40. [CrossRef]
30. Loew, A.; Mauser, W. Generation of geometrically and radiometrically terrain corrected SAR image products. *Remote Sens. Environ.* **2007**, *106*, 337–349. [CrossRef]
31. Loncar, M.; Leblon, B.; Richardson, A.; Bourgeau-Chavez, L.L.; Amishev, D. Comparison of L-Band ALOS-2 PALSAR-2 images for fuel moisture discrimination in mountainous forests. *Can. J. Remote Sens.* **2026**, *52*, 2684082. [CrossRef]
32. Van Zyl, J.J.; Zebker, H.A.; Elachi, C. Imaging radar polarization signatures: Theory and observations. *Radio Sci.* **1987**, *22*, 529–543. [CrossRef]
33. Touzi, R.; Goze, S.; Le Toan, T.; Lopes, A.; Mougin, E. Polarimetric discriminators for SAR images. *IEEE Trans. Geosci. Remote Sens.* **1992**, *30*, 973–980. [CrossRef]
34. Touzi, R.; Omari, K.; Sleep, B.; Jiao, X. Scattered and received wave polarization optimization for enhanced peatland classification and fire danger assessment using polarimetric PALSAR. *IEEE J. Sel. Top. Appl. Earth Obs. Remote Sens.* **2018**, *11*, 4452–4477. [CrossRef]

35. Hajnsek, I.; Pottier, E.; Cloude, S.R. Inversion of surface parameters from polarimetric SAR. *IEEE Trans. Geosci. Remote Sens.* **2003**, *41*, 727–744. [CrossRef]
36. Cloude, S.R.; Pottier, E. An entropy based classification scheme for land applications of polarimetric SAR. *IEEE Trans. Geosci. Remote Sens.* **1997**, *35*, 68–78. [CrossRef]
37. Xie, Q.; Wang, J.; Liao, C.; Lopez-Sanchez, J.M.; Fu, H.; Liu, X. On the use of Neumann decomposition for crop classification using multi-temporal RADARSAT-2 polarimetric SAR data. *Remote Sens.* **2019**, *11*, 776. [CrossRef]
38. Trisasongko, B.H. The use of polarimetric SAR data for forest disturbance monitoring. *Sens. Imaging* **2010**, *11*, 1–13. [CrossRef]
39. Zhang, L.; Wang, R.; Chai, H.; Lv, X. A polarimetric decomposition and copula quantile regression approach for soil moisture estimation from Radarsat-2 data over vegetated areas. *IEEE J. Sel. Top. Appl. Earth Obs. Remote Sens.* **2023**, *16*, 3405–3417. [CrossRef]
40. Xie, Z.; Zhu, W.; He, B.; Qiao, K.; Zhan, P.; Huang, X. A background-free phenology index for improved monitoring of vegetation phenology. *Agric. For. Meteorol.* **2022**, *315*, 108826. [CrossRef]
41. Girardin, M.P.; Tardif, J.; Flannigan, M.D.; Wotton, B.M.; Bergeron, Y. Trends and periodicities in the Canadian Drought Code and their relationships with atmospheric circulation for the southern Canadian boreal forest. *Can. J. For. Res.* **2004**, *34*, 103–119. [CrossRef]
42. Girardin, M.P.; Wotton, B.M. Summer moisture and wildfire risks across Canada. *J. Appl. Meteorol. Climatol.* **2009**, *48*, 517–533. [CrossRef]
43. Lavalle, M.; Wright, T. Absolute Radiometric and Polarimetric Calibration of ALOS PALSAR Products Generated Within ADEN. 2009. Available online: https://earth.esa.int/eogateway/documents/20142/37627/ALOS-PALSAR-calibration-products-ADEN.pdf (accessed on 14 September 2024).
44. Meyer, F.J.; Nicoll, B. Prediction, detection, and correction of Faraday rotation in full-polarimetric L-band SAR data. *IEEE Trans. Geosci. Remote Sens.* **2008**, *46*, 3076–3086. [CrossRef]
45. Lee, J.S.; Wen, J.H.; Ainsworth, T.L.; Chen, K.S.; Chen, A.J. Improved Sigma filter for speckle filtering of SAR imagery. *IEEE Trans. Geosci. Remote Sens.* **2009**, *47*, 202–213. [CrossRef]
46. Liaw, A.; Wiener, M. Classification and Regression by randomForest. *R News* **2002**, *2*, 18–22.
47. Breiman, L. Random forests. *Mach. Learn.* **2001**, *45*, 5–32. [CrossRef]
48. Shahriari, M.A.; Aghighi, H.; Azadbakht, M.; Ashourloo, D.; Matkan, A.A.; Brakhasi, F.; Walker, J.P. Soil moisture estimation using combined SAR and optical imagery: Application of seasonal machine learning algorithms. *Adv. Space Res.* **2025**, *75*, 6207–6221. [CrossRef]
49. Akhavan, Z.; Hasanlou, M.; Hosseini, M.; McNairn, H. Decomposition-Based Soil Moisture Estimation Using UAVSAR Fully Polarimetric Images. *Agronomy* **2021**, *11*, 145. [CrossRef]
50. Ji, Y.; Huang, J.; Ju, Y.; Guo, S.; Yue, C. Forest structure dependency analysis of L-band SAR backscatter. *PeerJ* **2020**, *30*, e10055. [CrossRef]
51. Benesty, J.; Chen, J.; Huang, Y.; Cohen, I. Pearson Correlation Coefficient. In *Noise Reduction in Speech Processing*; Springer Topics in Signal Processing; Springer: Berlin/Heidelberg, Germany, 2009; Volume 2, pp. 1–4. [CrossRef]
52. Johnson, G.L.; Hanson, C.L. Topographic and atmospheric influences on precipitation variability over a mountainous watershed. *J. Appl. Meteorol.* **1995**, *34*, 68–87. [CrossRef]
53. Bourgeau-Chavez, L.L.; Hanes, C.; Billmire, M.; Bosse, K.; Battaglia, M.J.; Colliander, A. Assessing SMAP for enhanced wildfire danger prediction in boreal-Arctic ecosystems. *Remote Sens. Appl. Soc. Environ.* **2026**, *41*, 101881. [CrossRef]
54. LaRocque, A.; Phiri, C.; Leblon, B.; Pirotti, F.; Connor, K.; Hanson, A. Wetland mapping with Landsat 8 OLI, Sentinel-1, ALOS-1 PALSAR, and LiDAR data in Southern New Brunswick, Canada. *Remote Sens.* **2020**, *12*, 2095. [CrossRef]
55. Dann, J.; Bennett, K.E.; Bolton, W.R.; Wilson, C.J. Factors Controlling a Synthetic Aperture Radar (SAR) Derived Root-Zone Soil Moisture Product over The Seward Peninsula of Alaska. *Remote Sens.* **2022**, *14*, 4927. [CrossRef]
56. Schönbrodt-Stitt, S.; Ahmadian, N.; Kurtenbach, M.; Conrad, C.; Romano, N.; Bogena, H.R.; Vereecken, H.; Nasta, P. Statistical exploration of SENTINEL-1 data, terrain parameters, and in-situ data for estimating the near-surface soil moisture in a Mediterranean agroecosystem. *Front. Water* **2021**, *3*, 655837. [CrossRef]
57. Prichard, S.J.; Nemens, D.G.; Kennedy, M.C.; Thoreson, J.; Satterfield, L.C.; Eagle, P.C.; Rowell, E.M.; Hudak, A.T.; Sanchez-Lopez, N. Forest floor properties in pine forests of the southeastern and western United States. *Fire Ecol.* **2025**, *21*, 85. [CrossRef]
58. Kurum, M.; Kim, S.-B.; Akbar, R.; Cosh, M.H. Surface soil moisture retrievals under forest canopy for L-band SAR observations across a wide range of incidence angles by inverting a physical scattering model. *IEEE J. Sel. Top. Appl. Earth Obs. Remote Sens.* **2021**, *14*, 1741–1753. [CrossRef]
59. Shi, J.; Wang, J.; Hsu, A.Y.; O'Neill, P.E.; Engman, E.T. Estimation of bare surface soil moisture and surface roughness parameter using L-band SAR image data. *IEEE Trans. Geosci. Remote Sens.* **1997**, *35*, 1254–1266. [CrossRef]
60. Kasischke, E.S.; Tanase, M.A.; Bourgeau-Chavez, L.L.; Borr, M. Soil moisture limitations on monitoring boreal forest regrowth using spaceborne L-band SAR data. *Remote Sens. Environ.* **2011**, *115*, 227–232. [CrossRef]

61. Yu, Y.; Saatchi, S. Sensitivity of L-band backscatter to aboveground biomass of global forests. *Remote Sens*. **2016**, *8*, 522. [CrossRef]
62. Kim, S.-B.; Xu, X.-L.; Kraatz, S.; Colliander, A.; Cosh, M.H.; Kelly, V.; Siqueira, P. Soil moisture estimates using L-band airborne SAR over forests replicating NISAR observations. *IEEE J. Sel. Top. Appl. Earth Obs. Remote Sens*. **2025**, *18*, 7364–7373. [CrossRef]
63. Hollaus, M.; Aubrecht, C.; Höfle, B.; Steinnocher, K.; Wagner, W. Roughness mapping on various vertical scales based on full-waveform airborne laser scanning data. *Remote Sens*. **2011**, *3*, 503–523. [CrossRef]
64. Borsah, A.A.; Nazeer, M.; Wong, M.S. LIDAR-based forest biomass remote sensing: A review of metrics, methods, and assessment criteria for the selection of allometric equations. *Forests* **2023**, *14*, 2095. [CrossRef]
65. Lim, K.; Treitz, P.; Wulder, M.; St-Onge, B.; Flood, M. LiDAR remote sensing of forest structure. *Prog. Phys. Geogr.* **2003**, *27*, 88–106. [CrossRef]
66. Latifi, H.; Heurich, M.; Hartig, F.; Müller, J.; Krzystek, P.; Jehl, H.; Dech, S. Estimating over- and understorey canopy density of temperate mixed stands by airborne LiDAR data. *Forestry* **2016**, *89*, 69–81. [CrossRef]
67. Tabatabaeenejad, A.; Burgin, M.; Moghaddam, M. Potential of L-band radar for retrieval of canopy and subcanopy parameters of boreal forests. *IEEE Trans. Geosci. Remote Sens*. **2012**, *50*, 2150–2160. [CrossRef]
68. Danson, F.M.; Bowyer, P. Estimating live fuel moisture content from remotely sensed reflectance. *Remote Sens. Environ*. **2004**, *92*, 209–221. [CrossRef]
69. Qui, J.; Crow, W.T.; Wagner, W.; Zhao, T. Effect of vegetation index choice on soil moisture retrievals via the synergistic use of synthetic aperture radar and optical remote sensing. *Int. J. Appl. Earth Obs. Geoinf.* **2019**, *80*, 47–57. [CrossRef]

Disclaimer/Publisher's Note: The statements, opinions and data contained in all publications are solely those of the individual author(s) and contributor(s) and not of MDPI and/or the editor(s). MDPI and/or the editor(s) disclaim responsibility for any injury to people or property resulting from any ideas, methods, instructions or products referred to in the content.